Multipole order in two-dimensional altermagnets

Tenta Tani^{1,*} and Ulrich Zülicke^{2,†}

¹Department of Physics, The University of Osaka, Toyonaka, Osaka 560-0043, Japan
²MacDiarmid Institute, School of Chemical and Physical Sciences,
Victoria University of Wellington, PO Box 600, Wellington 6140, New Zealand
(Dated: July 25, 2025)

We theoretically investigate the magnetic-multipole orders in two-dimensional (2D) altermagnets, focusing on two representative models: a generic minimal three-site model, and a four-site model representative of monolayer FeSe. We construct low-energy effective Hamiltonians for both systems and calculate their respective multipole indicators to characterize the underlying magnetic order. Our analysis reveals an intriguing contrast between the two systems. We find that the generic minimal model exhibits the expected non-zero magnetic-octupole order. In the monolayer-FeSe model, however, the magnetic-octupole order vanishes globally, and a magnetic-hexadecapole order is present instead. The emergence of altermagnetic splitting in the band structure then arises via the interplay with a sublattice-isospin degree of freedom. Our work demonstrates how the classification and comprehensive understanding of 2D altermagnetic materials transcends bulk descriptions.

I. INTRODUCTION

Altermagnetism [1–4] has recently been introduced as a term to designate magnetically ordered materials that have no bulk magnetization but still exhibit spin splitting in the electronic band structure. Altermagnets are thus different from ferromagnets (which have a finite spontaneous magnetization and associated uniform exchange spin splitting of electron states) and the more ordinary antiferromagnets (which also lack a bulk magnetization but retain spin degeneracy in their band structure because time inversion combined with a translation or with space inversion remains a good symmetry).

Physical ramifications of altermagnetism are currently attracting considerable attention. The altermagnetic properties of several materials have been intensively investigated, including RuO₂ [5–9], MnTe [10–12], and CrSb [13–15]. For example, spin-to-charge conversion [7], thermal transport [8], and magnons [5] have been examined for RuO₂. Two-dimensional (2D) altermagnets are also increasingly coming into focus [16–19], with proposed materials examples including MnPSe₃ [20], Cr₂SO [21] and V₂SeTeO [22].

Conceptually, altermagnetism in bulk materials can be understood as a manifestation of hidden magnetic-multipole order [23–25]. In contrast to ferromagnets that are characterized by a macroscopic magnetic-dipole density (the magnetization), altermagnets have been shown to exhibit spontaneous ordering of higher-odd-order magnetic multipoles such as octupoles, triakontadipoles, etc.

In the present work, we investigate the connection to multipole order for low-dimensional altermagnet realizations. For this purpose, we consider two specific microscopic models. The first one is the minimal model for a 2D altermagnet introduced in Ref. [16] and illustrated in Fig. 1(a), with two magnetic atoms and an additional nonmagnetic atom per unit cell. The second model is representative of monolayer FeSe, which was shown to become an altermagnet in the presence of a perpendicular electric field [20]. See Fig. 2 for the corresponding crystal structure, which can be regarded just as the minimal model [16] displayed in Fig. 1(a) with one additional nonmagnetic atom in the unit cell.

We treat each model by first diagonalizing their respective tight-binding Hamiltonians that include nearest-neighbor and next-nearest-neighbor hopping terms, as well as local exchange-energy splittings at the magnetic sites. (For the case of monolayer FeSe, the electrostatic potential arising from the perpendicular electric field is also included.) This yields the known altermagnetic band structures for the two model systems [16, 20]. We then derive a faithful effective envelope-function-Hamiltonian description for the low-energy subbands by adapting the standard subband- $\mathbf{k} \cdot \mathbf{p}$ theory that was originally devised for treating 2D-electron states in semiconductor heterostructures [26, 27]. We identify terms in the effective low-energy model Hamiltonian that are represen-

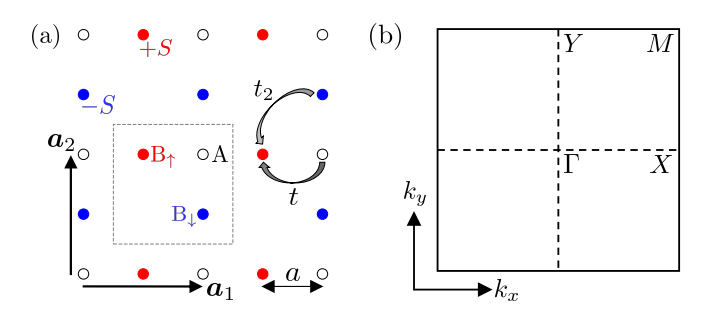


FIG. 1. Minimal model for a 2D altermagnet [16]. (a) Square lattice with sites having a localized spin-up (red), spin-down (blue), or no magnetization (white). Primitive lattice vectors a_1, a_2 are shown as black arrows, and a (next-)nearest-neighbor hopping process with parameter t (t_2) is depicted by gray arrows. (b) First Brillouin zone of the 2D square lattice.

^{*} tenta.tani@qp.phys.sci.osaka-u.ac.jp

[†] uli.zuelicke@vuw.ac.nz

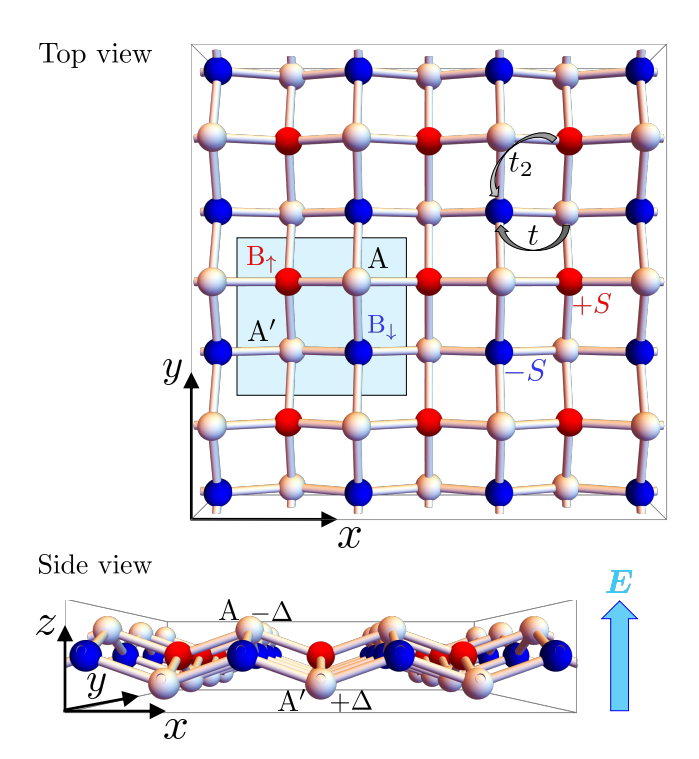


FIG. 2. Structure representing monolayer FeSe. The unit cell (indicated by the cyan square) contains two Fe atoms (red and blue) and two Se atoms (white). In the tight-binding model, nearest-neighbor (t) and second-nearest-neighbor (t_2) hopping parameters are included. The Fe sites are assumed to have localized spins $\pm S$. By applying a perpendicluar electric field \boldsymbol{E} , the two Se sites acquire different potentials $\pm \Delta$.

tative of the hidden multipole order and derive the associated band-structure indicators using the method proposed in Sec. II E of Ref. [24]. This enables quantification of higher-order magnetic-multipole densities in the 2D altermagnetic structures considered here. Our analytical results reveal intriguing parametric dependencies of the multipole order.

The remainder of this Article is organized as follows. Section II is devoted to analyzing the minimal model for 2D altermagnets proposed in Ref. [16] and shown in Fig. 1(a). We derive the effective low-energy effective model for the band structure and obtain the indicator of the magnetic-octupole density that is associated with altermagnetism in this structure. The magnitude of the latter is then calculated both analytically and numerically. In Sec. III, we consider the simple model for 2D FeSe depicted in Fig. 2, and derive its effective model. Surprisingly, we find that the magnetic-octuple density vanishes globally, while a magnetic-hexadecapole density represents hidden order in the FeSe system. Altermagnetic band splitting is shown to arise from the intricate interplay between the hexadecapolar order and the perpendicular electric field. Finally, Sec. IV presents our conclusions.

II. MAGNETIC-OCTUPOLE ORDER IN A MINIMAL MODEL FOR 2D ALTERMAGNETS

To obtain generic insights into 2D altermagnets, we consider the minimal model proposed in Ref. [16]. As shown in Fig. 1(a), the model consists of a nonmagnetic site A and two magnetic sites B_{\uparrow} and B_{\downarrow} . The unit cell is indicated by the dashed square, and the primitive lattice vectors are $\mathbf{a}_1 = (2a,0)$, $\mathbf{a}_2 = (0,2a)$. In momentum space, reciprocal-lattice vectors are given by $\mathbf{b}_1 = (\pi/a,0)$, $\mathbf{b}_2 = (0,\pi/a)$. In Fig. 1(b), the first Brillouin zone with labelled high-symmetry points is shown.

The electron Hamiltonian of the model is given by

$$\mathcal{H} = \sum_{\sigma=\pm} \left(t \sum_{\langle i,j \rangle} c_{i,\sigma}^{\dagger} c_{j,\sigma} + t_2 \sum_{\langle \langle i,j \rangle \rangle} c_{i,\sigma}^{\dagger} c_{j,\sigma} - J_{\text{sd}} \sigma \sum_{i} S_i c_{i,\sigma}^{\dagger} c_{i,\sigma} \right),$$

$$(1)$$

where $c_{i,\sigma}^{\dagger}$ and $c_{i,\sigma}$ are the creation and anihilation operators of an electron with spin $\sigma=\pm 1$ at lattice site i. The parameter t quantifies hopping between nearestneighbor pairs $\langle i,j \rangle$, and t_2 is the corresponding hopping parameter between second-nearest-neighbor sites $\langle \langle i,j \rangle \rangle$. Examples for these hopping processes are illustrated in Fig. 1(a). The prefactor $J_{\rm sd}$ of the third term is the exchange coupling between localized and itinerant electrons. The respective localized-electron spins of atoms on the A, B_{\(\gamma\)}, and B_{\(\gamma\)} sites are given by $S_i=0$, S, and -S, respectively. Taking Bloch states $\{|A\rangle, |B_{\uparrow}\rangle, |B_{\downarrow}\rangle\}$ as the basis, the Bloch Hamiltonian is written as

$$H(\mathbf{k}, \sigma) = \begin{pmatrix} 0 & 2\cos k_x & 2\cos k_y \\ 2\cos k_x & -J\sigma & 4t_2\cos k_x\cos k_y \\ 2\cos k_y & 4t_2\cos k_x\cos k_y & J\sigma \end{pmatrix},$$
(2)

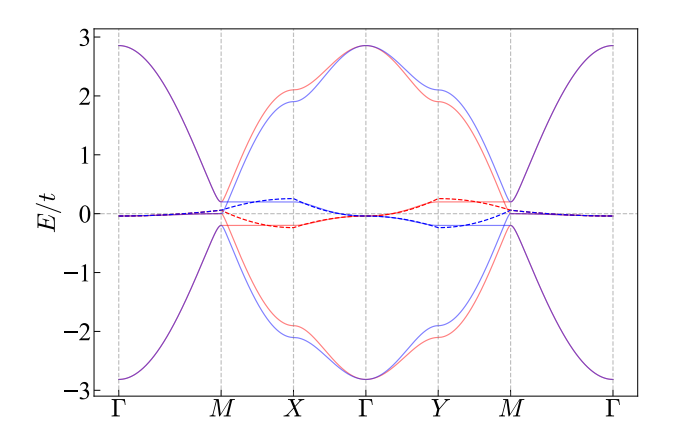


FIG. 3. Band structure for the minimal 2D-altermagnet model. The six bands plotted as the solid lines are calculated from the original Hamiltonian (2). The dispersions shown as dashed lines are obtained from the effective Hamiltonian (7). The red (blue) color indicates spin-up (spin-down) bands. The hopping parameters are set to be $J/t = 0.2, t_2/t = 0.01$.

where $J = J_{\rm sd}S$, and we set a = 1, t = 1 for simplicity. From this Hamiltonian, the electronic band structure is obtained as shown in Fig. 3 by the solid curves, using parameters J/t = 0.2 and $t_2/t = 0.01$. Red (blue) curves are for the spin-up (down) sector; these exhibit the altermagnetic spin splitting.

We now focus on the low-energy spectrum around the Γ point. An effective two-band Hamiltonian H_{eff} describing states near the Fermi level is constructed as follows. Exactly at the Γ point, the Hamiltonian (2) becomes

$$H_{\Gamma}(\sigma) = \begin{pmatrix} 0 & 2 & 2 \\ 2 & -J\sigma & 4t_2 \\ 2 & 4t_2 & J\sigma \end{pmatrix} . \tag{3}$$

If we set $t_2=0$, H_{Γ} can be analytically diagonalized. Assuming further $J\ll 1$ and neglecting $\mathcal{O}(J^2)$ terms, the eigenenergies are $E_1=0$, $E_2=-2\sqrt{2}$ and $E_3=2\sqrt{2}$. We transform the original Hamiltonian (2) to this band basis. The unitary matrix U for this transformation reads

$$U = \frac{1}{4} \begin{pmatrix} -\sqrt{2}J\sigma & -2\sqrt{2} - J\sigma & 2\sqrt{2} - J\sigma \\ -2\sqrt{2} & 2 + \sqrt{2}J\sigma & 2 - \sqrt{2}J\sigma \\ 2\sqrt{2} & 2 & 2 \end{pmatrix} . \tag{4}$$

Hence, the Hamiltonian in the new basis is obtained by $H'(\mathbf{k}, \sigma) = U^{\dagger}H(\mathbf{k}, \sigma)U$, which can be written as

$$H'(\mathbf{k}, \sigma) =$$

$$\begin{pmatrix}
-4t_2C_xC_y + J\sigma(C_x - C_y) & C_x - C_y + \frac{J\sigma}{\sqrt{2}}(1 - C_y) & -C_x + C_y + \frac{J\sigma}{\sqrt{2}}(1 - C_y) \\
C_x - C_y + \frac{J\sigma}{\sqrt{2}}(1 - C_y) & -\sqrt{2}(C_x + C_y) + 2t_2C_xC_y - \frac{J}{2}(3C_x + C_y) & 2t_2C_xC_y + \frac{J}{2}(C_x - C_y) \\
-C_x + C_y + \frac{J\sigma}{\sqrt{2}}(1 - C_y) & 2t_2C_xC_y + \frac{J}{2}(C_x - C_y) & \sqrt{2}(C_x + C_y) + 2t_2C_xC_y - \frac{J}{2}(3C_x + C_y)
\end{pmatrix},$$
(5)

where we used the abbreviations $C_x \equiv \cos k_x$ and $C_y \equiv \cos k_y$. When we further neglect $\mathcal{O}(J)$ and $\mathcal{O}(t_2)$ corrections to terms of $\mathcal{O}(1)$, we find

$$H'(\mathbf{k},\sigma) = \begin{pmatrix} -4t_2C_xC_y & C_x - C_y & -C_x + C_y \\ C_x - C_y & -\sqrt{2}(C_x + C_y) & 2t_2C_xC_y \\ -C_x + C_y & 2t_2C_xC_y & \sqrt{2}(C_x + C_y) \end{pmatrix} + J\sigma(C_x - C_y) \begin{pmatrix} 1 & 0 & 0 \\ 0 & 0 & 1/2 \\ 0 & 1/2 & 0 \end{pmatrix}.$$
(6)

In Eq. (6), the coupling between the $E = \mathcal{O}(t_2) \approx 0$ band and the bands with energies $|E| \approx 2\sqrt{2}$ is negligible in the vicinity of the Γ point, and the effective low-energy Hamiltonian is found as

$$H_{\text{eff}}(\mathbf{k}) = J\sigma_z(\cos k_x - \cos k_y) - 4t_2 \cos k_x \cos k_y \approx -\frac{J}{2} \,\sigma_z(k_x^2 - k_y^2) + 4t_2(\mathbf{k}^2/2 - 1) \ .$$
 (7)

Here σ_z denotes the Pauli matrix in spin space. The band structure obtained from this effective Hamiltonian is shown by the dashed curves in Fig. 3, where the red (blue) color corresponds to the spin-up (spin-down) electron states. We find that the effective bands fit the original dispersions fairly well and reproduce the altermagnetic spin-splitting. The spin-dependent Fermi surface of the model is depicted in Fig. 4(a), for $J < 4t_2$. The shapes of the Fermi surfaces are ellipses with a semimajor axis $k_{\rm F>} = [2/(1+J/4t_2)]^{1/2}$ and a semi-minor axis $k_{\rm F<} = [2/(1-J/4t_2)]^{1/2}$.

The connection between altermagnetism and multipole order is embodied in the spin-splitting term $\propto \sigma_z(k_x^2 - k_y^2)$ in the Hamiltonian (7). Specifically, the quantity

$$\mathcal{I}^{(\mathrm{m},3)}(\boldsymbol{k},\sigma) = \sigma(k_x^2 - k_y^2) \tag{8}$$

constitutes the band-structure indicator for a magneticoctupole density [24, 28] that is compatible with the system's magnetic-point-group symmetry $D_{4h}(D_{2h})$ [16]. The indicator's expectation value is straightforwardly calculated as

$$\langle \mathcal{I}^{(m,3)} \rangle = \sum_{\sigma} \int_{BZ} \frac{d\mathbf{k}}{(2\pi)^2} \mathcal{I}^{(m,3)}(\mathbf{k}, \sigma) f(E_{\mathbf{k}\sigma})$$
$$= \int_{BZ} \frac{d\mathbf{k}}{(2\pi)^2} (k_x^2 - k_y^2) [f(E_{\mathbf{k}+}) - f(E_{\mathbf{k}-})],$$
(9)

where f(E) is the Fermi distribution function and $E_{k\sigma}$ the band dispersions close to the Fermi energy.

The expectation value $\langle \mathcal{I}^{(m,3)} \rangle$ directly quantifies the magnetic-octupole density present in the system. (This is entirely analogous to how a finite expectation value of $\mathcal{I}^{(m,1)} = \sigma$ quantifies the magnetization. Obviously, $\langle \mathcal{I}^{(m,1)} \rangle \equiv 0$ in the present case.) We now calculate $\langle \mathcal{I}^{(m,3)} \rangle$ in the zero-temperature limit, where the difference of Fermi functions in the expression (9) is finite only for states occupied by either spin-up or spin-down electrons. Considering the shape of the Fermi surface [Fig. 4(a)], the four purple regions \mathcal{D}_1 to \mathcal{D}_4 contribute equally. Thus, Eq. (9) can be rewritten as

$$\langle \mathcal{I}^{(m,3)} \rangle = \frac{4}{(2\pi)^2} \int_{\mathcal{D}_1} d\mathbf{k} \ (k_x^2 - k_y^2) \ .$$
 (10)

To obtain an approximate analytical expression, we only

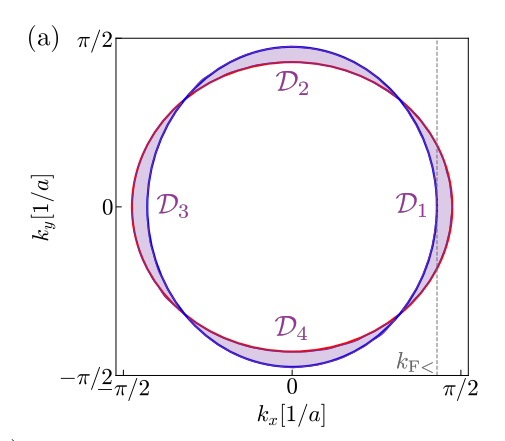
integrate over the region with $k_x > k_{\rm F}$ [see the gray

vertical line in Fig. 4(a)], which is a good approximation for larger J. After some computations, we find

$$\langle \mathcal{I}^{(m,3)} \rangle = \frac{1}{(2\pi)^2} \left[\left(\frac{\pi}{2} - \arcsin \frac{k_{F<}}{k_{F>}} \right) k_{F<} k_{F>} (k_{F>} + k_{F<}) (k_{F>} - k_{F<}) - \frac{k_{F<}^2}{3} \sqrt{1 - \frac{k_{F<}^2}{k_{F>}^2}} \left(k_{F<}^2 - 3k_{F>}^2 + \frac{2k_{F<}^4}{k_{F>}^2} \right) \right] . \tag{11}$$

In Fig. 4(b), we compare the numerical result (9) (black curve) and the analytical result (11) (red curve). The agreement between both is good for larger $J/4t_2$, as expected from the approximation used in the analytical calculation. Deviations become apparent in the small-J regime ($J/4t_2 \ll 1$), where we have

$$k_{\rm F>} \approx \frac{\sqrt{2}}{a} \left(1 + \frac{J/4t_2}{2} \right) , k_{\rm F<} \approx \frac{\sqrt{2}}{a} \left(1 - \frac{J/4t_2}{2} \right) ,$$
 (12)



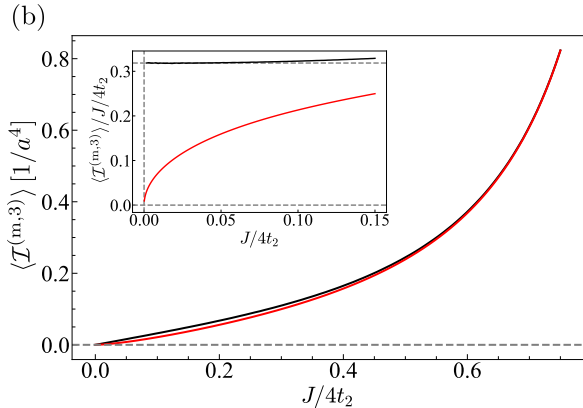


FIG. 4. (a) Fermi surfaces for spin-up (red) and spin-down (blue) states for the effective low-energy Hamitonian (7) derived for the generic 2D-altermagnet model [16] with parameters $J/4t_2 = 0.1$. Purple shading indicates the four regions with spin-polarized occupation. (b) Expectation value of the magnetic-octupole indicator $\langle \mathcal{I}^{(\mathrm{m},3)} \rangle$. The black (red) curve plots the numerical (analytical) result.

so that Eq. (11) reduces to

$$\langle \mathcal{I}^{(m,3)} \rangle \approx \frac{16\sqrt{2}}{3\pi^2 a^4} \left(\frac{J}{4t_2}\right)^{3/2} .$$
 (13)

As seen in the inset of Fig. 4, the asymptotic behavior of the numerical result is $\langle \mathcal{I}^{(m,3)} \rangle \propto J/(4t_2)$, and this is not reproduced by the analytical form (13). This discrepancy arises because the area left out of the integration range in the analytical calculation becomes significant in the small-J limit.

III. ALTERMAGNETIC MONOLAYER FeSe

In this section, we investigate monolayer FeSe. Its crystal structure is shown in Fig. 2. It has co-planar magnetic (Fe) sites and a buckling that renders the two Se sites in the unit cell inequivalent. As was done in Ref. [20], we assume checkerboard antiferromagnetic order to be present. The system is then characterized by the magnetic point group $C_{4h}(S_4)$, which has the combination of space inversion and time inversion as a good symmetry. As a result, the band dispersions are spin-degenerate and asymmetric around the Γ point. Application of a perpendicular electric field was shown to render the material an altermagnet [20].

We construct a tight-binding model for checkerboard-antiferromagnetic FeSe simply by adding an additional nonmagnetic site A' to the minimal 2D-altermagnet model discussed in Sec. II. An external perpendicular electric field is introduced via onsite potentials $\pm \Delta$ on the Se sites. We thus obtain a 4×4 Bloch Hamiltonian,

$$H(\mathbf{k}, \sigma) = \begin{pmatrix} -\Delta & 0 & 2\cos k_x & 2\cos k_y \\ 0 & \Delta & 2\cos k_y & 2\cos k_x \\ 2\cos k_x & 2\cos k_y & -J\sigma & 4t_2\cos k_x\cos k_y \\ 2\cos k_y & 2\cos k_x & 4t_2\cos k_x\cos k_y & J\sigma \end{pmatrix},$$
(14)

with basis states $\{|A\rangle, |A'\rangle, |B_{\uparrow}\rangle, |B_{\downarrow}\rangle\}$. The band structure calculated from this Hamiltonian for some sample parameters is plotted by the solid curves in Fig. 5. Around the M point, this model reproduces the DFT band structure calculated in Ref. [20].

At the M point, the Hamiltonian (14) is diagonal with eigenenergies $[E_{1\sigma}^{(0)},E_{2\sigma}^{(0)},E_{3\sigma}^{(0)},E_{4\sigma}^{(0)}]=[-\Delta,\Delta,-J\sigma,J\sigma].$

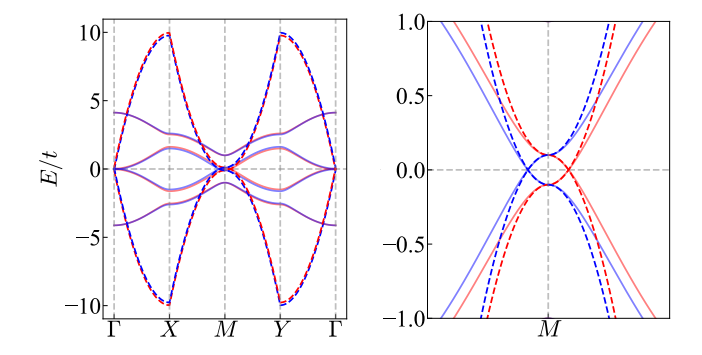


FIG. 5. Band structure of the four-site model for monolayer FeSe. The eight bands depicted by the solid lines are calculated from the original Hamiltonian (14), while the four bands shown by the dashed lines are obtained from the effective Hamiltonian (18). Red (blue) color represents the spin-up (spin-down) dispersion. The right panel is a magnification around the M point. Parameters used in the calculation are J/t=1, $t_2/t=0$, and $\Delta/t=0.1$.

In order to derive a low-energy effective Hamiltonian, we apply second-order perturbation theory to these eigenstates. This yields the energy dispersions

$$E_{ki\sigma} = E_{i\sigma}^{(0)} + \sum_{j \neq i} \frac{\langle u_i^{(0)} | H' | u_j^{(0)} \rangle}{E_{i\sigma}^{(0)} - E_{j\sigma}^{(0)}} , \qquad (15)$$

for i=1,2,3,4. H' is defined via $H=H_0+H'$ and $H_0=H(\pmb{k}=M)$. $|u_i^{(0)}\rangle$ is the ith eigenvector of H_0 .

Here we are interested in the two bands with i=1,2, which represent the band structure closest to the Fermi energy E=0. When we relabel i=1,2 in terms of a pseudospin quantum number $\tau=\pm 1$, we have

$$E_{\mathbf{k}\tau\sigma} = \tau \left[\Delta + 4 \frac{(\Delta + J\sigma)\cos^2 k_x + (\Delta - J\sigma)\cos^2 k_y}{\Delta^2 - J^2} \right].$$
(16)

We can derive an effective Hamiltonian considering the limit of a small perpendicular electric field. For $J \gg \Delta$,

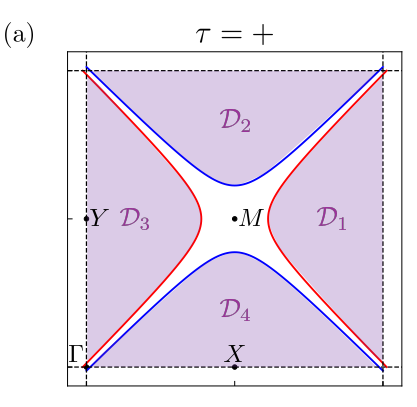
$$H_{\text{eff}}(\mathbf{k}) = \tau_z [\Delta - (4/J)\sigma_z(\cos^2 k_x - \cos^2 k_y)] , \quad (17)$$

where τ_z is the Pauli matrix in the low-energy two-band space. When we take the M point to be the origin of k space, we have

$$H_{\text{eff}}(\mathbf{k}) = \tau_z [\Delta - (4/J)\sigma_z (k_x^2 - k_y^2)],$$
 (18)

for small k. Plotting the band dispersions for the effective Hamiltonian (18) by dashed lines in Fig. 5, we see that they coincide with the original low-energy bands close to the M point.

The Fermi surface calculated from the effective Hamiltonian (18) for the $\tau=+$ band is shown in Fig. 6(a). It consists of hyperbolas $k_x^2/k_{\rm F0}^2-k_y^2/k_{\rm F0}^2=\pm 1$, where the +/- signs are for the spin-up/-down electrons, respectively. Here we introduced the scale $k_{\rm F0}=\sqrt{J\Delta}/2$.



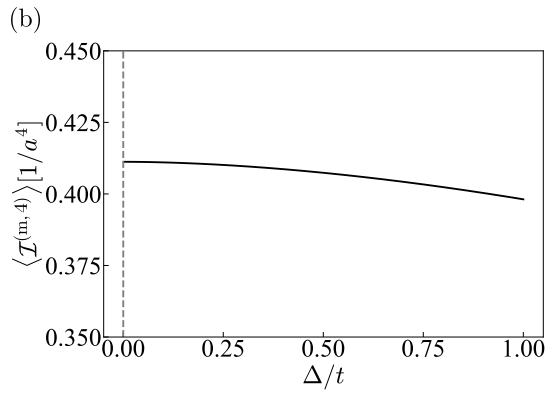


FIG. 6. (a) Fermi surfaces of the minimal model for FeSe at the M point. Here we plot the $\tau=+$ sector only. Regions \mathcal{D}_1 and \mathcal{D}_3 (\mathcal{D}_2 and \mathcal{D}_4) are occupied by spin-up(-down) states. Parameters used are J/t=1, $t_2/t=0$, and $\Delta/t=0.5$. (b) Expectation value $\langle \mathcal{I}^{(m,4)} \rangle$ of the magnetic-hexadecapole indicator (19), plotted as a function of the electric-potential magnitude Δ .

Spin-up (spin-down) states are occupied in the region \mathcal{D}_1 and \mathcal{D}_3 (\mathcal{D}_2 and \mathcal{D}_4).

In the effective Hamiltonian (18), σ_z corresponds to the electron spin, whereas τ_z is a sublattice-pseudospin degree of freedom distinguishing the Se sites $\{A, A'\}$. Therefore, τ_z has the characteristics of the spatial coordinate z, including its transformational properties under space inversion (odd) and time inversion (even). Consequently, the quantity

$$\mathcal{I}^{(\mathrm{m},4)}(\boldsymbol{k},\tau,\sigma) = \tau \,\sigma \,(k_x^2 - k_y^2) \tag{19}$$

constitutes a band-structure indicator for a rank-4 multipole that is odd under both space inversion and time inversion, i.e., a magnetic hexadecapole.

The possibility of real-space quantities, such as sublattice-related pseudospins, appearing in effective Hamiltonians and energy dispersions for 2D systems enlarges the palette of band-structure indicators for multipole order beyond those that have previously been constructed for 3D crystals [24, 28]. Magnetic-hexadecapole order is a case in point. In a bulk crystalline solid, its indicator must be an odd-order polynomial in wave-vector

components [28] and cannot involve spin. The fact that, for a 2D system, the combination $\tau_z \, \sigma_z$ transforms like a wave-vector component enables a substitution $k_j \to \tau \, \sigma$, leading to the form as given in (19). As a result, the connection between multipole order and spin splitting in the band structure turns out to be much richer for 2D systems. For more explicit illustration of this point, we now characterize both the magnetic octupole and the magnetic hexadecapole order in the FeSe model system.

A. Magnetic octupole

The indicator for a macroscopic magnetic-octupole density is given in Eq. (8). Its expectation value for the FeSe system is obtained by evaluating

$$\langle \mathcal{I}^{(\mathrm{m},3)} \rangle = \sum_{\tau\sigma} \int_{\mathrm{BZ}} \frac{d\mathbf{k}}{(2\pi)^2} \mathcal{I}^{(\mathrm{m},3)}(\mathbf{k},\sigma) f(E_{\mathbf{k}\tau\sigma}) .$$
 (20)

At zero temperature, Eq. (18) implies $\sum_{\tau\sigma} \sigma f(E_{k\tau\sigma}) \equiv \sum_{\sigma} \sigma = 0$. Hence, the integrand from Eq. (20) vanishes identically, and so does $\langle \mathcal{I}^{(\mathrm{m},3)} \rangle$. This result means that

the contributions to a magnetic-octupole density from the two sublattices $\tau=\pm$ cancel out.

B. Magnetic hexadecapole

The expectation value of the magnetic-hexadecapole indicator (19) for the FeSe system is obtained from

$$\langle \mathcal{I}^{(\mathrm{m},4)} \rangle = \sum_{\tau,\sigma} \int_{\mathrm{BZ}} \frac{d\mathbf{k}}{(2\pi)^2} \mathcal{I}^{(\mathrm{m},4)}(\mathbf{k},\tau,\sigma) f(E_{\mathbf{k}\tau\sigma}).$$
 (21)

In this integral, contributions for $\tau = \pm$ do not cancel, as we find

$$\sum_{\tau\sigma} \tau \, \sigma \, f(E_{k\tau\sigma}) = 2 \sum_{\sigma} \sigma \, f(E_{k+\sigma}) \ . \tag{22}$$

Considering the shape of Fermi surfaces for the $\tau=+$ bands [Fig. 6(a)], the expectation value (21) is obtained via

$$\langle \mathcal{I}^{(m,4)} \rangle = \frac{8}{(2\pi)^2} \int_{\mathcal{D}_1} d\mathbf{k} \ (k_x^2 - k_y^2) \ ,$$
 (23)

since the four regions \mathcal{D}_1 to \mathcal{D}_4 contribute equally to the result. We can exactly integrate this to get an expression

$$\langle \mathcal{I}^{(\mathrm{m},4)} \rangle = \frac{k_{\mathrm{F}0}^4}{2\pi^2} \left[\frac{\pi}{6k_{\mathrm{F}0}a} \sqrt{\frac{\pi^2}{4k_{\mathrm{F}0}^2 a^2} - 1} \left(\frac{\pi^2}{k_{\mathrm{F}0}^2 a^2} + 2 \right) - 2\ln \left(\frac{\pi}{2k_{\mathrm{F}0}a} + \sqrt{\frac{\pi^2}{4k_{\mathrm{F}0}^2 a^2} - 1} \right) \right] . \tag{24}$$

The Δ -dependence of $\langle \mathcal{I}^{(m,4)} \rangle$ is plotted in Fig. 6(b). Note that it stays finite in the limit $\Delta=0$, i.e., it is a property of the FeSe crystal itself. However, the associated altermagnetic spin splitting emerges only for $\Delta \neq 0$ when the combined spin and sublattice-pseudospin degeneracy is lifted.

IV. CONCLUSION

We have investigated multipole order in a minimal model for generic 2D altermagnets, and for a model system representing monolayer FeSe. Consistent with crystal symmetry, the former is shown to exhibit magnetic-octupole order, whereas the latter hosts a macroscopic magnetic-hexadecapole density. Both orders are quantified based on their respective band-structure indicators, given in Eqs. (8) and (19), respectively.

In contrast to 3D crystals where magnetic-

hexadecapole order is indicated by band dispersions that are asymmetric in wave-vector components but always remain spin-degenerate, such order in a 2D system can give rise to altermagnetic spin splitting. We link such fundamental differences in physical ramifications for the same type of multipole order to the possibility to have 2D band-structure invariants that involve pseudospins that are equivalent to real-space (e.g., sublattice) positions. Future work could focus on incorporating more systematically any possible pseudospin degrees of freedom into the construction of band-structure indicators in 2D crystals.

ACKNOWLEDGMENTS

T.T. was supported by JSPS KAKENHI Grant No. JP23KJ1497.

^[1] L. Šmejkal, J. Sinova, and T. Jungwirth, Beyond conventional ferromagnetism and antiferromagnetism: A phase

- Phys. Rev. X 12, 031042 (2022).
- [2] L. Šmejkal, J. Sinova, and T. Jungwirth, Emerging research landscape of altermagnetism, Phys. Rev. X 12, 040501 (2022).
- [3] M. Roig, A. Kreisel, Y. Yu, B. M. Andersen, and D. F. Agterberg, Minimal models for altermagnetism, Phys. Rev. B 110, 144412 (2024).
- [4] C. Song, H. Bai, Z. Zhou, L. Han, H. Reichlova, J. H. Dil, J. Liu, X. Chen, and F. Pan, Altermagnets as a new class of functional materials, Nat. Rev. Mater. 10, 473 (2025).
- [5] L. Šmejkal, A. Marmodoro, K.-H. Ahn, R. González-Hernández, I. Turek, S. Mankovsky, H. Ebert, S. W. D'Souza, O. Šipr, J. Sinova, and T. Jungwirth, Chiral magnons in altermagnetic RuO₂, Phys. Rev. Lett. 131, 256703 (2023).
- [6] S. W. Lovesey, D. D. Khalyavin, and G. van der Laan, Magnetic structure of RuO₂ in view of altermagnetism, Phys. Rev. B 108, L121103 (2023).
- [7] H. Bai, Y. C. Zhang, Y. J. Zhou, P. Chen, C. H. Wan, L. Han, W. X. Zhu, S. X. Liang, Y. C. Su, X. F. Han, F. Pan, and C. Song, Efficient spin-to-charge conversion via altermagnetic spin splitting effect in antiferromagnet RuO₂, Phys. Rev. Lett. 130, 216701 (2023).
- [8] X. Zhou, W. Feng, R.-W. Zhang, L. Šmejkal, J. Sinova, Y. Mokrousov, and Y. Yao, Crystal thermal transport in altermagnetic RuO₂, Phys. Rev. Lett. 132, 056701 (2024).
- [9] O. Fedchenko, J. Minár, A. Akashdeep, S. W. D'Souza, D. Vasilyev, O. Tkach, L. Odenbreit, Q. Nguyen, D. Kutnyakhov, N. Wind, L. Wenthaus, M. Scholz, K. Rossnagel, M. Hoesch, M. Aeschlimann, B. Stadtmüller, M. Kläui, G. Schönhense, T. Jungwirth, A. B. Hellenes, G. Jakob, L. Šmejkal, J. Sinova, and H.-J. Elmers, Observation of time-reversal symmetry breaking in the band structure of altermagnetic RuO₂, Sci. Adv. 10, eadj4883 (2024).
- [10] I. I. Mazin, Altermagnetism in MnTe: Origin, predicted manifestations, and routes to detwinning, Phys. Rev. B 107, L100418 (2023).
- [11] S. Lee, S. Lee, S. Jung, J. Jung, D. Kim, Y. Lee, B. Seok, J. Kim, B. G. Park, L. Šmejkal, C.-J. Kang, and C. Kim, Broken Kramers degeneracy in altermagnetic MnTe, Phys. Rev. Lett. 132, 036702 (2024).
- [12] T. Aoyama and K. Ohgushi, Piezomagnetic properties in altermagnetic MnTe, Phys. Rev. Mater. 8, L041402 (2024).
- [13] J. Ding, Z. Jiang, X. Chen, Z. Tao, Z. Liu, T. Li, J. Liu, J. Sun, J. Cheng, J. Liu, Y. Yang, R. Zhang, L. Deng, W. Jing, Y. Huang, Y. Shi, M. Ye, S. Qiao, Y. Wang, Y. Guo, D. Feng, and D. Shen, Large band splitting in g-wave altermagnet CrSb, Phys. Rev. Lett. 133, 206401

- (2024).
- [14] S. Reimers, L. Odenbreit, L. Šmejkal, V. N. Strocov, P. Constantinou, A. B. Hellenes, R. Jaeschke Ubiergo, W. H. Campos, V. K. Bharadwaj, A. Chakraborty, T. Denneulin, W. Shi, R. E. Dunin-Borkowski, S. Das, M. Kläui, J. Sinova, and M. Jourdan, Direct observation of altermagnetic band splitting in CrSb thin films, Nat. Commun. 15, 2116 (2024).
- [15] Z. Zhou, X. Cheng, M. Hu, R. Chu, H. Bai, L. Han, J. Liu, F. Pan, and C. Song, Manipulation of the altermagnetic order in CrSb via crystal symmetry, Nature (London) 638, 645 (2025).
- [16] B. Brekke, A. Brataas, and A. Sudbø, Two-dimensional altermagnets: Superconductivity in a minimal microscopic model, Phys. Rev. B 108, 224421 (2023).
- [17] J. Sødequist and T. Olsen, Two-dimensional altermagnets from high throughput computational screening: Symmetry requirements, chiral magnons, and spin-orbit effects, Appl. Phys. Lett. 124, 182409 (2024).
- [18] S. Zeng and Y.-J. Zhao, Description of two-dimensional altermagnetism: Categorization using spin group theory, Phys. Rev. B 110, 054406 (2024).
- [19] A. Asgharpour, B. Koopmans, and R. A. Duine, Synthetic altermagnets, Phys. Rev. B 111, 094412 (2025).
- [20] I. Mazin, R. González-Hernández, and L. Šmejkal, Induced monolayer altermagnetism in MnP(S,Se)₃ and FeSe, arXiv:2309.02355 (2023).
- [21] S.-D. Guo, X.-S. Guo, K. Cheng, K. Wang, and Y. S. Ang, Piezoelectric altermagnetism and spin-valley polarization in Janus monolayer Cr₂SO, Appl. Phys. Lett. 123, 082401 (2023).
- [22] Y. Zhu, T. Chen, Y. Li, L. Qiao, X. Ma, C. Liu, T. Hu, H. Gao, and W. Ren, Multipiezo effect in altermagnetic V₂SeTeO monolayer, Nano Lett. 24, 472 (2024).
- [23] S. Hayami, Y. Yanagi, and H. Kusunose, Momentum-dependent spin splitting by collinear antiferromagnetic ordering, J. Phys. Soc. Jpn. 88, 123702 (2019).
- [24] R. Winkler and U. Zülicke, Theory of electric, magnetic, and toroidal polarizations in crystalline solids with applications to hexagonal lonsdaleite and cubic diamond, Phys. Rev. B 107, 155201 (2023).
- [25] S. Bhowal and N. A. Spaldin, Ferroically ordered magnetic octupoles in d-wave altermagnets, Phys. Rev. X 14, 011019 (2024).
- [26] D. A. Broido and L. J. Sham, Effective masses of holes at GaAs-AlGaAs heterojunctions, Phys. Rev. B 31, 888 (1985).
- [27] S.-R. Eric Yang, D. A. Broido, and L. J. Sham, Holes at GaAs-Al_xGa_{1-x}As heterojunctions in magnetic fields, Phys. Rev. B 32, 6630 (1985).
- [28] R. Winkler and U. Zülicke, Standard model of electromagnetism and chirality in crystals, arXiv:2405.20940 (2025).